Transparent and Conformal Microcoil Arrays for Spatially Selective Neuronal Activation

Vineeth Raghuram[1,2,3], Aditya D. Datye[3], Shelley I. Fried[1,2,3,], and Brian P. Timko[1,*]*

1. Tufts University, Dept. of Biomedical Engineering, Medford, MA 02155, USA
2. Boston VA Healthcare System, Boston, MA 02130, USA
3. Dept. of Neurosurgery, Massachusetts General Hospital, Harvard Medical School, Boston, MA, 02114, USA

*Corresponding author e-mails: Fried.Shelley@mgh.harvard.edu, brian.timko@tufts.edu

Abstract

Magnetic stimulation represents a compelling modality for achieving neuronal activation with high spatial resolution and low toxicity. Stimulation coils can be designed to achieve localized, spatially asymmetric fields that target neurons of a particular orientation. Furthermore, these devices may be encapsulated within biopolymers thereby avoiding direct metal/tissue interfaces that could induce chronic inflammation and glial scarring. Herein, we report a multiplexed microcoil array for localized activation of cortical neurons and retinal ganglion cells. We designed a computational model that related the activation function to the geometry and arrangement of coils, and selected a geometry with a region of activation <50 µm wide. We then fabricated SU8/Cu/SU8 tri-layer devices which were flexible, transparent and conformal and featured four individually-addressable microcoil stimulation elements. Interfaced with ex vivo cortex or retina slices from GCaMP6-transfected mice, we observed that individual neurons located within 40 µm of the element tip could be activated repeatedly and in a dose (power) dependent fashion. Taken together, these results highlight the potential of magnetic stimulation devices for brain-machine interfaces and could open new routes toward bioelectronic therapies including prosthetic vision devices.

Introduction

Neural prostheses that can effectively activate the cortex offer a promising solution to treat a variety of neurological disorders (Jang et al., 2019; Raspopovic et al., 2021) and restore sensory functionality. These devices typically consist of an intracortically implanted multi-electrode array (MEA) which aims to create localized regions of neural activation by electrically stimulating pyramidal neurons proximal to the electrode site. While the current progress in prosthetic design/development is encouraging, the quality of perception (e.g visual, tactile) elicited by these implants can be quite variable (Butovas and Schwarz, 2003; Histed et al., 2009; Lewis et al., 2015). The variability in the responses produced by these devices is most likely a result of the non-specific activation of multiple cell-types by artificial stimulation with an MEA. The next generation of chronic cortical implants must incorporate improved stimulation strategies that can selectively target specific neuronal populations while simultaneously avoiding others.

One of the challenges in the design of effective neural prostheses has been the ability to confine neuronal activation to precise regions; this is especially relevant with devices that target sensory portions of the cortex where the ability to exert fine spatiotemporal control can be directly correlated to overall performance. Recent efforts (Lee et al., 2016, 2018; Lee and Fried, 2017) have shown that magnetic stimulation of cortical neurons using microcoils may offer several key advantages over conventional electrodes when targeting the cortex. These include, for example, the ability to generate localized, spatially asymmetric electric fields that can be used to selectively target specific populations of neurons. In contrast to the large, radial spread of activation generated by conventional microelectrodes, the electric fields produced by microcoils may be aligned to preferentially target vertically oriented pyramidal neurons while avoiding horizontally aligned passing axon fibers (Lee et al., 2016, 2018). This would be particularly beneficial in applications where focal activation is critical, such as the restoration of high acuity vision or in the stimulation of specific regions of the somatosensory cortex. A further advantage of magnetic stimulation is that magnetic fields readily pass through biological tissue and, as a result, could circumvent performance defects due to glial encapsulation and scarring (Williams et al., 2007; Kozai et al., 2014).

Prior studies have validated, using both computational and experimental approaches, (1) the ability of a single microcoil to generate small, focal regions of activation (Lee et al., 2016), and (2) the effects of varying coil shape/design, on the both the spatial selectivity and strength of activation (Lee et al., 2018). While devices that consist of a single microcoil may be useful in targeting one isolated region of the cortex, the ability to focally activate multiple cortical columns, or specific cortical layers, either in synchrony or in temporally modulated intervals (interleaved), would improve the translational value for clinical applications where the creation of multiple regions of neural activity is the goal. As a step towards achieving this goal, we focused on developing an array of four individually accessible micro coils that would be capable of simultaneously generating distinct regions of focal neuronal activation.

The focus of this study was the design and validation of flexible, transparent, and biocompatible microcoil arrays made from SU-8 (an epoxy based negative photoresist) for use within in-vitro cortical slice electrophysiology experiments. Unlike traditional silicon based Michigan/Utah-type multi-electrode arrays (Badi et al., 2003; Cheung, 2007), coils placed within an insulated substrate (like SU8) would avoid direct contact between the metal layer and brain tissue. Additionally, the use of insulators that have enhanced biocompatibility would help to mitigate the long-term inflammatory tissue responses that are usually associated with chronically implanted devices (Polikov et al., 2005; Grill et al., 2009). Prior microcoil-based studies (Lee et al., 2016; Lee and Fried, 2017) primarily used SiO_2 as a substrate due to its strength and durability, thereby facilitating insertion of these probes into mouse cortical slices. However, the mechanical mismatch between rigid silicon based devices (Young's modulus >100GPa) and brain tissue (Young's modulus ~ 1 kPa), has been shown to induce adverse immune reactions (Kozai et al., 2014; Salatino et al., 2017; Lecomte et al., 2018), and as a result may not be the best material for chronic applications. Here, we investigated SU-8 as substrate material for microcoil arrays, as it offers several significant advantages over conventional materials including silicon substrates or platinum-iridium electrodes. These include a greater biocompatibility, enhanced flexibility, and significantly less mechanical mismatch (Young's modulus of SU-8 can be modulated from 1-10 GPa) with the surrounding brain tissue (Nemani et

al., 2013; Huang et al., 2014; Matarèse et al., 2018). In addition, SU-8 can be made (1) stretchable using specific geometries like serpentine structures as well as (2) into mesh-like grids that which be seamlessly injected into brain tissue (reviewed in (Song et al., 2020)). SU-8 is also photo-curable, enabling lithography of complex patterns onto the substrate material; this would mean the ability to readily incorporate different coil shapes (Lee et al., 2018) within a single array. Finally, SU-8 is a highly transparent material that would allow clear visualization of neuronal morphology and physiological responses during fluorescence imaging studies. While the use of SU-8 as an effective substrate and insulating layer for "mesh-like" neural recording probes has recently been demonstrated in both the cortex (Zhou et al., 2017) and retina (Hong et al., 2018), our platform represents the first instance of its use for micro-magnetic stimulation of neurons.

Our experimental approach in this study involved (1) selecting an optimal candidate microcoil geometry for use within a multicoil array based on computational modeling of electrical fields, (2) developing a fabrication protocol to produce microcoils supported by flexible substrates, and (3) experimentally validating the effectiveness our coil array. These arrays will provide a framework to perform further stimulation studies that would investigate the interactions between the fields generated by multiple individual coils and explore how these fields would affect different populations of activated neurons in different cortical regions.

Methods

Microfabrication Protocol

All photoresists and developers were used as received from Kayaku Advanced Materials, Westborough, MA. (1) A 50 nm sacrificial layer of germanium (Ge) was sputtered on onto silicon/silicon oxide substrates (300nm, Cat. 2525). (2) The bottom passivation layer of the device was composed of 10 μm thick SU8 (SU8 2010) that was spin coated, patterned with UV photolithography (16s @ 15mW/cm^2) and developed with SU-8 developer for 1 minute. (3) The metal layer was defined using a LOR20B/S1813 bi-layer stack followed by UV exposure (12s @ 15mW/cm^2), developed using CD-26, metallized with a 1 μm layer of copper deposited by thermal evaporation (LC Technology Solutions, Salisbury MA), and lifted off with Remover 1165 at room temperature. (4) The top passivation layer of the device was composed of 20 μm thick SU8 (SU8 2025) that was spin coated and patterned with UV photolithography (21s @ 15mW/cm^2) with a develop time of 5 minutes. (5) Devices were lifted off by dissolving the Ge layer in DI water at 80°C for up to 48 hours. Next, the interconnect section (Figure 2B, top right) was adhered onto a rigid plastic backing and wires were attached to the exposed copper pads using silver epoxy paste (CW2400, Chemtronics) (Figure 2B,left). The resistance of each device including interconnects was 40-60 Ω and was consistent between consecutive trials.

Modeling

We developed a computational model to characterize the induced electric fields arising from the flow of electrical current in an array of microcoils consisting of different coil geometries (rectangular, U-shaped, and V-shaped). We utilized a charge-based boundary element fast multipole method (BEM-FMM) toolkit to calculate the induced electric fields within the tissue. Unlike the commonly-applied finite element method (FEM), BEM-FMM operates directly on tissue conductivity boundary surfaces, thus eliminating the need for volumetric meshing (Makarov et al., 2020). After the solution at the tissue boundaries is determined through an iterative process, the magnetic and electric fields from the flow of current through an insulated coil can be evaluated in 3D space, similar to general-purpose FEM software. An important advantage of the BEM-FMM approach is that it allows unconstrained numerical field resolution near tissue interfaces, and thus the induced fields and their spatial gradients can be calculated

at a high resolution without the secondary interpolations required for volumetric FEM-based solvers. The BEM-FMM approach is also more computationally efficient compared to existing software packages (Makarov et al., 2020).The region surrounding the array (600 × 600 × 600 μm cube) was modeled as a homogenous, isotropic medium with the properties of grey matter (electrical conductivity: σ = 0.276 S/m) (Wagner et al., 2006), similar to the approach used earlier by members of our group to characterize the spatial extent of intracortical microcoil-based stimulation (Lee et al., 2018). After the modeling setup was defined, the BEM-FMM toolkit was utilized to calculate the electric field inside the tissue (with a spatial resolution of 1 μm) in response to an applied AC current.

In the quasistatic limit, which is commonly used when modeling electromagnetic fields in biological tissues and is considered valid for frequencies up to ~10 kHz (Janssen et al., 2015), the total induced electric field is given by:

$$\boldsymbol{E} = \left(-\frac{\partial \boldsymbol{A}}{\partial t}\right) + (-\nabla\varphi)$$

where $\boldsymbol{A}$ is the magnetic vector potential and φ represents the electric potential due to surface charge redistribution at tissue conductivity boundaries (Miranda et al., 2003). The secondary field $(-\nabla\varphi)$ can be ignored if the primary field $\left(-\frac{\partial \boldsymbol{A}}{\partial t}\right)$ is parallel to the air-tissue boundary (Wang et al., 2018) as we have done here. The primary field was obtained by discretizing the coil into small, straight elements of current $i_j(t)$ with orientation $\boldsymbol{s}_j$ and center coordinate $\boldsymbol{p}_j$. The magnetic vector potential created by a current element at an observation point $\boldsymbol{c}_i$ is given by:

$$\boldsymbol{A}(\boldsymbol{c}_i, t) = \frac{\mu_0}{4\pi} \frac{i_j(t)\, \boldsymbol{s}_j}{|\boldsymbol{c}_i - \boldsymbol{p}_j|}$$

where μ_0 is the magnetic permeability of vacuum (Makarov et al., 2020). The corresponding electric field generated by the current element is:

$$\boldsymbol{E}(\boldsymbol{c}_i, t) = -\frac{\partial \boldsymbol{A}(\boldsymbol{c}_i, t)}{\partial t} = -\frac{\mu_0}{4\pi} \frac{\partial i_j(t)}{\partial t} \frac{\boldsymbol{s}_j}{|\boldsymbol{c}_i - \boldsymbol{p}_j|}$$

The contributions from each element j of the coil are summed to find the total electric field distribution. All calculations were performed at an instant in time when the rate of change of current (di/dt) through the coil was 1A/μs which is a representative value that has been utilized

in prior computational studies involving magnetic stimulation (Roth and Basser, 1990). Simulations were performed on an Intel Core i7-6700 CPU (3.40 GHz, 32 GB RAM, 4 cores) with an average computation time of ~1 minute for each simulated microcoil array.

In-vitro brain slice experiments

Electrophysiological recordings were performed using brain slices prepared from 30- to 50-day-old mice (C57BL/6J; The Jackson Laboratory), similar to previously described methods from our group (Lee et al., 2016, 2018).The care and use of animals followed all federal and institutional guidelines, the Institutional Animal Care and Use Committees of the Boston Veterans Affairs (VA) Healthcare System, and the Subcommittee on Research Animal Care of the Massachusetts General Hospital. The mice were deeply anesthetized with isoflurane and decapitated. The brains were removed immediately after death, and a section of the brain containing the visual cortex V1 (0.5-1mm anterior from the lambdoid suture) was isolated on ice in a 0° to 5°C oxygenated solution containing 1.25 mM NaH_2PO_4, 2.5mM KCl, 25mM $NaHCO_3$, 1 mM $MgCl_2$, 25 mM glucose, and 225 mM sucrose, equilibrated with 95% O_2–5% CO_2 (pH 7.4). This cold solution, with a low sodium ion and without calcium ion content, improved tissue viability. In the same medium, 300- to 400-µm-thick coronal slices were prepared using a vibrating blade microtome (Vibratome 3000 Plus, Ted Pella Inc.) and were incubated at room temperature in an artificial cerebrospinal fluid (aCSF) solution containing 125 mM NaCl, 1.25 mM NaH_2PO_4, 2.5 mM KCl, 25 mM $NaHCO_3$, 1 mM $MgCl_2$, 2 mM $CaCl_2$, and 25 mM glucose, equilibrated with 95% O_2–5% CO_2 (pH 7.4). After a 2-hour recovery period, slices that contained V1 were transferred and mounted, caudal side down, to a plastic recording chamber (RC-27L,Warner Instruments, LLC) with a plastic slice anchor (SHD-27LP/2, Warner Instruments, LLC). The chamber was maintained at 30° ± 2°C and continuously superfused (3.3 ml/min) with oxygenated aCSF solution.

Patch Clamp Validation

A patch clamp amplifier (MultiClamp 700B, Molecular Devices) operating in voltage-clamp mode with a holding potential of 0 mV was used to measure the artifact signals that were generated during the passage of current through an individual coil for bench testing experiments. The

magnitude of the stimulus artifact (pA) was defined as the distance between positive and negative phases of the recorded signal.

Fluorescence Microscopy

Brain slices were prepared and maintained as described above and were then incubated in a dark room at room temperature in aCSF solution. After a 2-hour recovery period, slices that contained the primary visual cortex (V1) were transferred and mounted, caudal side down, to the plastic recording chamber (RC-27L) with a plastic slice anchor (SHD-27LP/2). Imaging was performed with a Nikon Eclipse FN1 microscope (Nikon Instruments Inc.) through a 20× 0.5 numerical aperture objective (Nikon Fluor 20× /0.50 water immersion objective). The excitation light source (X-Cite 120Q; Excelitas Technologies Corp.) was coupled to the epifluorescent port of the microscope. Calcium fluorescence changes were captured with a sCMOS camera (USB 3.1 Gen 1; 2048 x 2048; 30 frames/s; PCO.Panda 4.2). Images were recorded and then processed using image analysis software (ImageJ; National Institutes of Health). Outlines around the somas of individual pyramidal neurons were defined to create ROIs. The calcium fluorescence transients for individual neurons were calculated as $(\Delta F/F_0) = (F - F_0)/F_0$, where F_0 was the baseline fluorescence level calculated by averaging over 2s before the onset of stimulation, and subsequently normalized to max observed fluorescence change.

Data Analysis

MATLAB's 'fitnlm' function was utilized to fit each dose-response curve with a four-parameter sigmoidal function defined by $F'(I) = F'_{min} + (F'_{max} - F'_{min})/[1 + (I_{50}/I)\hat{}\beta]$, where $F' = (\Delta F/F_0)$ and β is the dynamic range. I_{50} is the current amplitude required to elicit 50% of the maximum fluorescence change; this was used as an estimate for the threshold of magnetic stimulation.

Results

Selecting microcoil geometry for multicoil array design

Confining neuronal activation to a specific region with microelectrodes has proven to be challenging as they generate large, spatially uniform electric field gradients that can activate

passing axon fibers (Lee et al., 2016, 2018; Lee and Fried, 2017). In contrast, microcoils produce localized asymmetric field gradients which can be manipulated to target specific populations of neurons while avoiding passing axons (Lee et al., 2016).

A previous study by members of our group utilized a computational model to characterize the field gradients and spatial spread of activation produced by different microcoil geometries (Lee et al., 2018). Because our goal was to characterize the effectiveness of microcoil arrays in creating multiple, distinct regions of neural activation, we developed a computational model using a MATLAB toolkit (Makarov et al., 2020) (Methods) to explore the interaction between the electric fields produced by two adjacent coils in the array (**Fig. 1**). Our goal for the model was to minimize the field interaction between adjacent coils, while also keeping the spacing between elements minimal enough to be able incorporate a greater number of channels. Three different microcoil geometries were tested: rectangular, U-shaped, and V-shaped (**Fig. 1A**). Similar to previous studies (Wagner et al., 2006; Bonmassar et al., 2012; Lee et al., 2018), the region surrounding the arrays was modeled as a homogenous, isotropic medium with the properties of grey matter. In order to isolate the effect of coil geometry, the distance between the vertical leads of the coils in each array was fixed at 100 μm and the rate of change of current through the individual coils in the arrays was 1 A/μs (direction of current in each coil is indicated by arrows).

Previous computational studies (Rattay, 1986; Basser et al., 1992; Esselle and Stuchly, 1992) have shown that the strength of the gradient of the electric field arising along the length of a targeted axon (referred to as the activating function (Rattay, 1986)) is a good predictor of the effectiveness of a given set of stimulating conditions. Because the axons of the targeted pyramidal neurons in the cortical slice are oriented in roughly the same (y-) direction (two examples are schematically depicted in green), we focused on analyzing the electric field gradient parallel to these axons $\left(\frac{dE_y}{dy}\right)$. Gradients were calculated along a plane 10 μm below the surface of the array and are plotted in color. Color map limits were fixed at +/-2000 V/m^2 in order to compare the gradients produced by different coil geometries; yellow and blue regions correspond to negative (< -2000 V/m^2) and positive (> +2000 V/m^2) gradients (respectively); axons that pass-through regions of stronger negative gradient are more likely to undergo depolarization and be activated.

When the array consisted of two adjacent rectangular coils (**Fig. 1A**, left), a single region of activation (yellow) was observed in the space between the coils. The width of this region was larger than the coil separation distance (100 μm). A region of activation with roughly the same size was produced by an array consisting of two U-shaped coils (**Fig. 1A**, middle). In contrast, an array of two V-shaped coils (**Fig. 1A**, right) produced two narrower and non-overlapping regions of activation, each confined to the tip of a coil. The relationship between coil geometry and the size of the region of activation was further explored by modeling a single coil and modifying the radius of curvature of its tip (i.e., a gradual transition from a V-shape to a U-shaped design) and calculating the width of the region of activation (where dEy/dy < -2000 V/m^2) (**Fig. 1B**). A smaller bend radius (as in the V-shaped design) was associated with a narrower region of activation. This trend is consistent with the analogous relationship between the radii of coils utilized in transcranial magnetic stimulation (TMS) and their induced fields: TMS coils with smaller dimensions generally produce electric fields with a smaller tangential spread (Deng et al., 2013).

These results demonstrate that, for a given coil separation distance, the array of V-shaped coils may be more effective in creating multiple, distinct regions of neural activation (**Fig. 1C**). In contrast, the overlapping regions of activation produced by the rectangular and U-shaped designs would reduce channel independence.

This may also be explained by the tendency for the electric field to decay sharply with distance away from the coil. Neglecting the effects of tissue conductivity inhomogeneities, the induced electric field at an observation point $\boldsymbol{r}$ produced by a small element of the coil can be approximated by $d\boldsymbol{E}(\boldsymbol{r},t) \approx -\frac{\mu_0}{4\pi}\frac{\partial I(t)}{\partial t}\frac{d\boldsymbol{l}}{|\boldsymbol{r}-\boldsymbol{s}|}$, where μ_0 is the permeability of vacuum, $\frac{\partial I(t)}{\partial t}$ is the rate of change of current through the coil, $\boldsymbol{s}$ is the position of the coil element, and $d\boldsymbol{l}$ is a differential vector along the direction of the coil (Esselle and Stuchly, 1992). The electric field at $\boldsymbol{r}$ is inversely proportional to the distance from the coil element $|\boldsymbol{r}-\boldsymbol{s}|$. Although the separation distance between the parallel leads in each coil is 100 μm, the geometry of the V-shaped design creates additional separation between the tips of the coils, leading to weaker (and therefore narrower) induced field gradients.

Because our goal is to minimize the overlap between the adjacent coils, while maintaining channel independence, we chose to design and fabricate a V-shaped array for use in subsequent

physiological experiments.

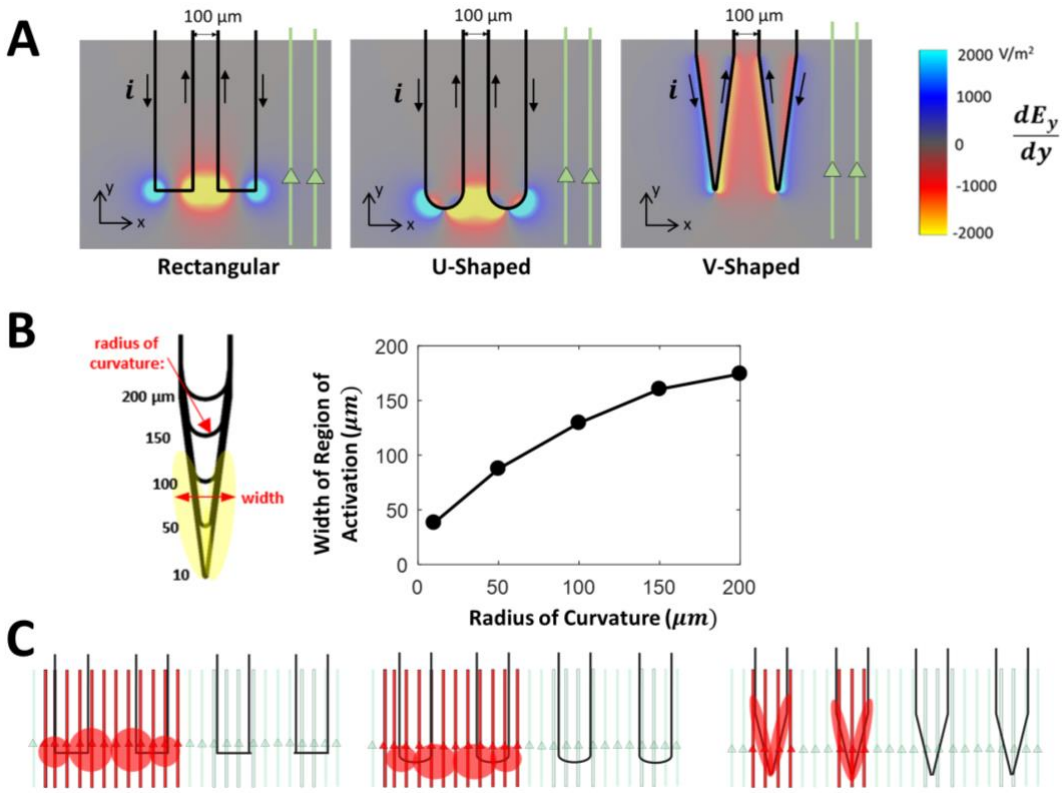

Figure 1: Computational modeling of microcoil array geometries and experimental schematic. (A) Heat maps depicting the induced electric field gradient produced by rectangular, U- and V-shaped geometries. Gradients are calculated on a plane that is 10 µm below the bottom edge of the array and with di/dt=1A/µs. Black arrows depict the directions of current through the coils. (B) *Left:* schematic illustration of a microcoil with a gradually increasing radius of curvature at its tip. *Right:* relationship between bend radius of the tip and width of the region of activation. C) Schematic illustration of pyramidal neuron axons (light green) interfaced with devices and corresponding activation regions (yellow) shown in panel a. Axons passing through regions of stronger gradient are more likely to be activated (red); hence, V-shaped devices are hypothesized to offer better spatial resolution.

Fabrication and assembly of flexible, transparent microcoil arrays

While earlier efforts have examined the ability of a single bend of a microwire to generate a small region of neuronal activation (Lee et al., 2016), the ability of multiple coils to generate multiple focal points of activation has yet to be investigated. The ability to focally activate multiple cortical columns, or specific cortical layers, either in synchrony or in temporally modulated intervals (interleaved), is essential to improve the translational value of a microcoil-based prosthetic in clinical applications where the creation of multiple independent regions of neural

activity is required for effective functionality– e.g, in a visual prosthesis that aims to create distinct shapes or spell out specific letters/words, corresponding to visual percepts.

As an initial step towards this goal**,** we designed and fabricated a multi-coil array to explore the interaction between neighboring coils and its capability in generating non overlapping regions of activation. Briefly, our design consisted of an array of 4 adjacent microcoils (Figure 2A), with the tips equally spaced 250µm apart. This distance was chosen as it is approximately the distance between adjacent cortical columns (Bonin et al., 2011). The V-shaped coil geometry that we implemented for each of the coils in our array has previously been shown to be effective for activating pyramidal neurons (Lee et al., 2018), and was found to produce minimal overlap of field gradients when compared to other geometries (Figure 1A).

We optimized a fabrication protocol (Figure 2B) to achieve an array of individually accessible microcoils on a flexible and transparent substrate. Our device consisted of Cu coils and interconnects sandwiched between two layers of SU-8, which functioned both as flexible support substrate and passivation layer. We implemented a series of eight interconnected copper pads, with each set of two adjacent pads corresponding to the signal and ground elements for an individual coil (Figure 2B). A distance of 3.5 cm between the rectangular layers of interconnects and the microcoils allowed for facile placement of the functional portion of the coil onto the microscope stage as well as sufficient distance between the base of the device and the chamber slide on which the tissue slice would be placed. The dimensions of the multi-coil array were specifically chosen for use in *in-vitro* electrophysiology experiments that would be used to assess functionality of the design. Given that the width of a typical adult mouse in-vitro cortical slice is around 4.5 mm and the total length between the edges of the substrate is about 1.3 mm (Figure 2C, bottom right), the multicoil array would occupy only about 30% of the tissue width and could be easily rotated to adapt to different slice orientations. As a typical pyramidal neuron has a soma diameter of around 20-25 µm, the distance between the coils should allow the visualization of activation up to 10 or 11 cells. We found that our fabrication protocol was able to consistently reproduce functional flexible multi-coil array devices which were robust across multiple consecutive experimental trials. Each device was tested before and after each physiological

experiment to ensure no leakage of electrical current from the coil into the brain tissue. To do this, coils were submerged in PBS solution and the DC impedance between one of the coil terminals and an electrode immersed in the solution were measured. In addition, the impedance between leads was found consistent when measured before and after experiments. To evaluate device transparency, we interfaced the array on-top of cortical tissue in both fluorescence (Figure 2D, left) and brightfield mode (Figure 2D, right) and found clear visualization of the tissue underneath the device. This provided further confirmation that our device would be suitable for large scale calcium imaging applications. While our preliminary design consisted of a 4x1 array of evenly spaced microcoils, we anticipate that our protocol (2A, see methods) may be easily adapted to expand the number, geometry, and spacing of coils placed within a single device .

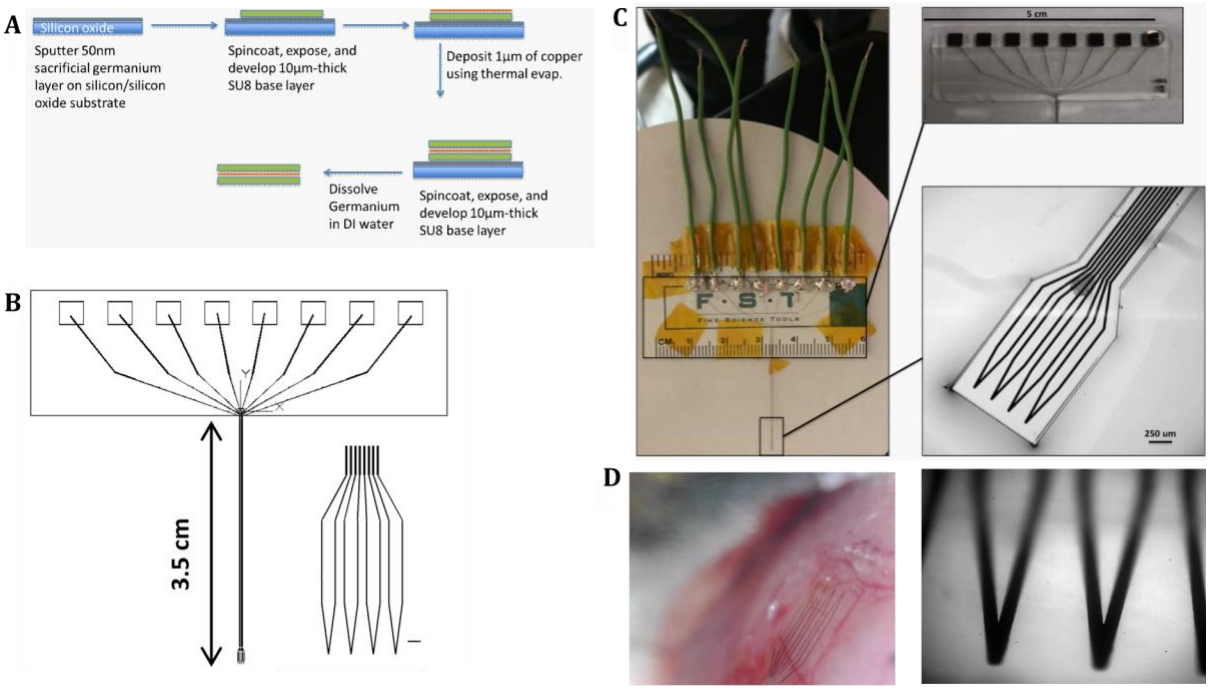

Figure 2: Fabrication and assembly of flexible microcoil devices – (A) Schematic of fabrication process. (B) Schematic of multicoil array for magnetic stimulation. Each pair of square pads corresponds to stimulation and ground elements for 1 coil (of total 4) with closeup of 4-coil array tip (right). Scale bar is 150 µm (C) Overview of assembled multicoil array. Wires are bonded to the exposed copper pads using silver epoxy. (insets) Photos of fabricated device detailing (top) 8 copper pads (3mm x 3mm) and (bottom) 4 stimulation coils. (D) Microcoil array interfaced on top of cortical tissue in fluorescence (left) and brightfield mode (right).

Microcoil functionality was confirmed by characterizing electrical artifacts produced during magnetic stimulation

We tested the functionality of the fabricated microcoils through two separate experiments. First, preliminary bench tests were performed to characterize the electrical signals generated by the devices. Second, *in-vitro* electrophysiology experiments were used to evaluate the neuronal response to magnetic stimulation. In this section, we will further describe the bench experiments that were used to measure the electrical artifacts resulting from the passing of electrical current through the individual coils. Briefly, we submerged the coil tips within a chamber slide containing PBS solution and placed a glass patch pipette approx. 5 µm above the plane of a single coil tip, as shown (Figure 3A). To drive the microcoil, we connected the output of a function generator to a 1000W audio amplifier (PB 717X, Pyramid Inc.) with a gain of 5.6V/V and a bandwidth of 70 kHz (Lee et al., 2016), and delivered continuous series ramp pulses with amplitudes ranging from 0 to 1500mV (output of function generator); the duration of both the rising and falling phases was 0.1ms (total 0.2 ms), there was a 5.2 ms interval between consecutive pulses (edge to edge distance) (Figure 3B).The resultant artifact (Figure 3C) measured at the patch pipette represents the current injected by the patch amplifier to offset the change in voltage at the pipette tip generated by the microcoil (see Methods). The artifact consisted of a biphasic waveform whose positive and negative phase corresponded to the rise and falling elements of the input ramp pulse (Figure 3C, right). Further, we found that the amplitude of the stimulus artifact increased linearly with the amplitude of the stimulus current (Figure 3D). The amplitude of the stimulus currents mentioned here, as well as the rest of the manuscript, refer to the output of the audio amplifier. These preliminary results were consistent with those reported previously (Lee et al., 2016; Lee and Fried, 2017).

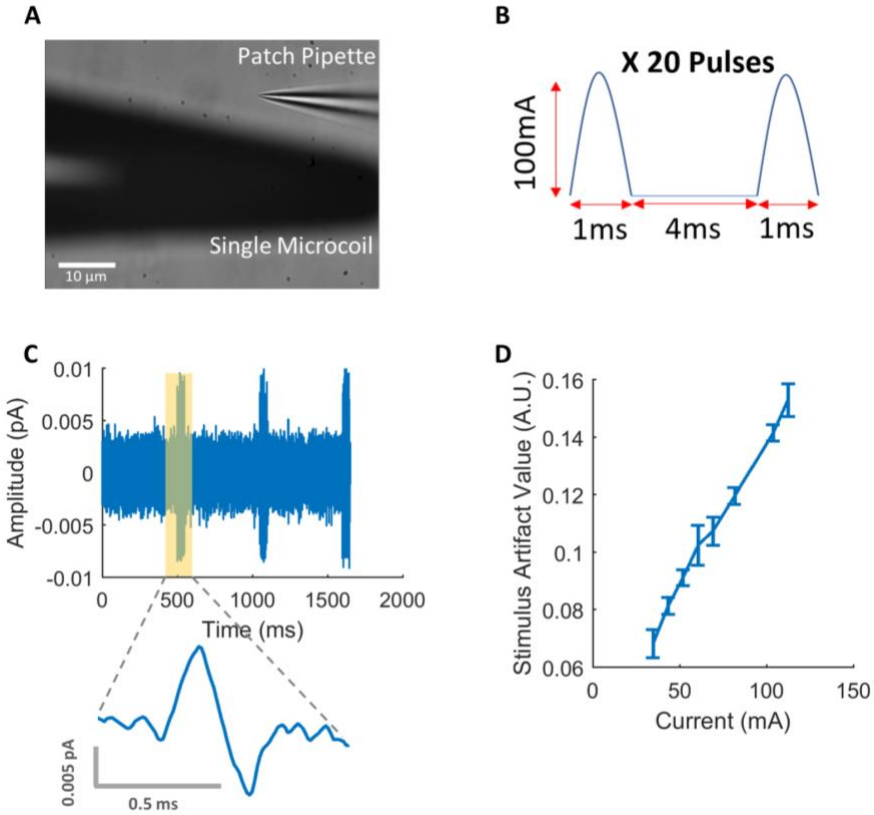

Figure 3: Electronic validation of flexible microcoil devices – (A) Placement of single coil next to patch pipette for recording artifact signals. (B) Parameters of half-sine waveforms delivered using MC stimulus package (C) (top) Example of electrical artifacts generated by magnetic stimulation in continuous mode. (bottom) Single biphasic stimulus artifact. (D) Plot of stimulus artifact magnitude vs. current through single microcoil for sinusoidal stimulus parameters. Error bars represent S.D., n=3.

Flexible microcoil arrays effectively activate CNS neurons

To determine whether the flexible microcoil array could activate neurons, we performed physiological experiments using brain slices obtained from the visual cortex of Thy-1 GCaMP6f mouse visual cortex. This mouse model was chosen as it possesses a genetically encoded calcium indicator that fluorescently labels several neuronal populations within the CNS (including pyramidal neurons in the cortex) and, as a result, has been used in previous studies involving the magnetic stimulation of neurons (Lee et al., 2016, 2018; Lee and Fried, 2017). The microcoil array was overlaid on the surface of a mouse cortical slice from the visual cortex (~300 µm thickness) so that the response of layer 5 pyramids neurons to magnetic stimulation could be visualized (Figure 4A). The use of a transparent substrate enables neural signals to be visualized between and around individual coil traces (Figure 4A). To observe activation of individual pyramidal neurons, we delivered a series of burst stimuli, each consisting of 20 waveforms (1ms duration)

with an inter-waveform interval of 4ms. These parameters are similar to those shown recently to drive V1 pyramidal neurons *in-vivo* (Ryu et al., 2020). There was a 500 ms interval between consecutive bursts (Figure 4B). The waveforms were half-sinusoidal (positive) in shape, each with an amplitude of 200 mA . Stimulus parameters (pulse frequency, shape, interpulse interval) were also based on previous studies (Lee et al., 2018; Ryu et al., 2020) while stimulus amplitude was varied to establish the minimum level at which a calcium imaging response was produced within individual cell bodies (identified during post-image processing). We utilized the NIH ImageJ/FIJI software package to quantify the change in fluorescence that was observed within a single cell close the tip of the stimulated coil. We found that individual stimuli each reliably elicited a neuronal calcium response (Figure 4C), thereby validating the ability of a single microcoil in our array to activate neurons.

To further test the functionality of our microcoil, we repeated the above experiments using the mouse retina and trying to activate retinal ganglion cells (RGCs). The microcoil array was placed on the top surface of a retinal explant, oriented so that the RGCs were directly underneath the coil traces (Figure 4D). To observe activation of RGCs, we delivered a series of burst stimuli, each consisting of 100 waveforms, through a single coil. Each burst was separated by a period of 1s (Figure 4E). The waveforms were triangular (positive) in shape, each at an amplitude of 100mA. Similar to our results with cortical neurons, we found that each of delivered stimuli reliably elicited a neuronal calcium response (Figure 4F).

To compare the response patterns generated with magnetic stimulation by microcoils vs. electric stimulation using microelectrodes, we repeated our experiments in the cortical slice using a single 10 kΩ PtIr microelectrode (Figure 4G). To observe activation of individual pyramidal neurons, we delivered a series of burst stimuli, each consisting of 20 square pulses (0.2 ms duration) with an interpulse interval of 9.6 ms. There was a 500 ms interval between consecutive bursts (Figure 4H). The pulses were biphasic square pulse in shape, each at an amplitude of 70 µA. Similar to the previously descried, stimulus parameters (pulse frequency, shape, interpulse interval) were chosen as a result of previous studies (Lee et al., 2016, 2018) while stimulus amplitude was chosen as a supra-threshold value. The activation pattern arising from electrodes was significantly different from microcoils and included greater activation of surrounding neuropil and somata (Figure 4G, right).

We also examined the relationship between the amplitude of magnetic stimulation and the fluorescence change of cortical neurons (**Fig. 5A**). Dose-response curves are shown for 11 cells, and the shaded error bars indicate the standard deviation across repeated trials (n = 3). Following the approach utilized by a previous study (Larsch et al., 2013), we used MATLAB to find the threshold of each dose-response curve (see Methods). We defined threshold (I_{50}) as the current amplitude required to elicit 50% of the maximum fluorescence change. The threshold for each cell was plotted with respect to its distance from the tip of the coil (**Fig. 5B**). The thresholds did not appear to correlate with the cell's distance from the coil (correlation coefficient: r = 0.22). However, given the small number of cells tested and possible convoluting factors such as cell type and morphology (Fried et al., 2009; Werginz et al., 2020; Raghuram et al., 2021) further experimentation is likely required to investigate this relationship. It is notable, however, that the change in fluorescence was confined to a small region near the tip of the coil; the maximum cell distance in which a fluorescence change was observed was 40 μm.

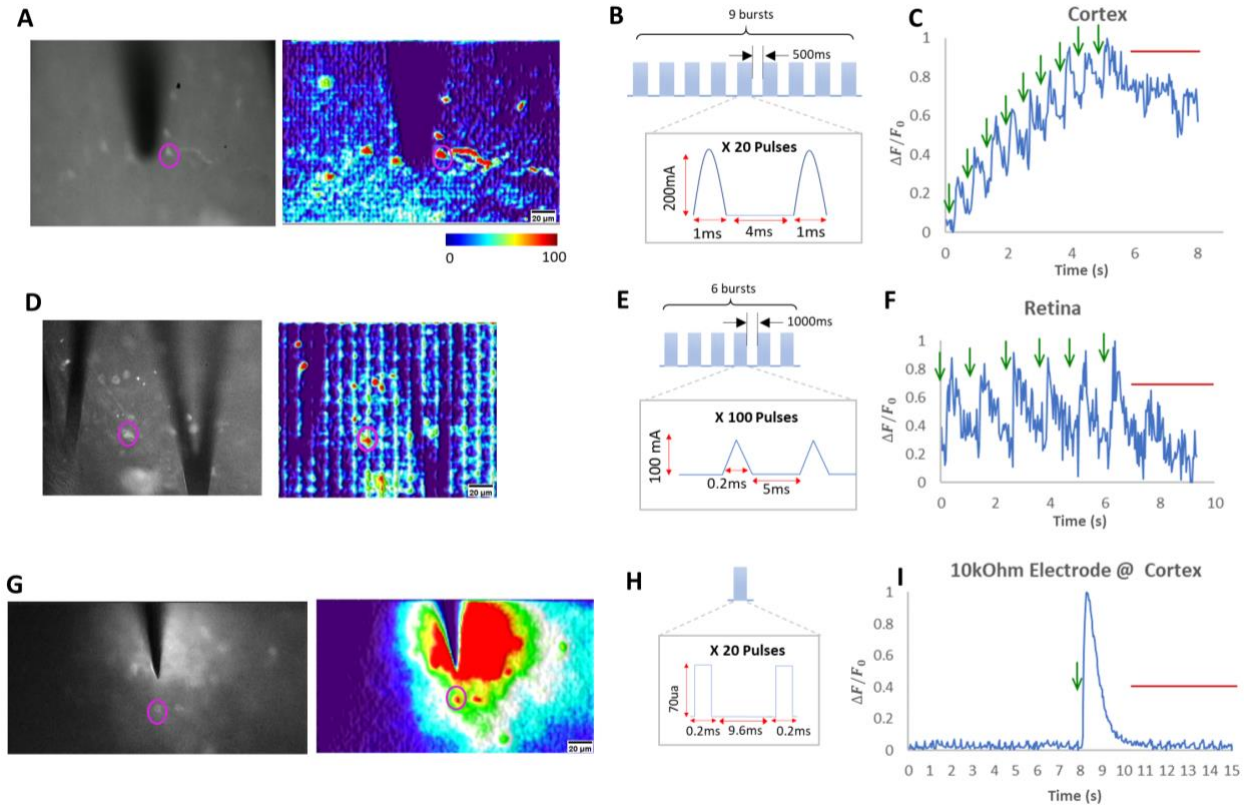

Figure 4: Interfacing flexible, transparent microcoils and microelectrode on wholemount mouse retina, cortex, and calcium imaging of neuronal activation(A) Close up of a single microcoil conformally placed on top of a mouse cortical slice in fluorescence mode (left) and heat-map of peak fluorescence change to stimulus(right). Purple circle indicates neuron in which fluorescence is analyzed below.(B) Schematic of burst stimulus waveform that was delivered to a single coil to activate cortical neurons. Each burst (9) consisted of 20 pulses, at 200 mA pulse amplitude

with 1ms duration, delivered at an interval of 4ms. (C) Calcium fluorescence change observed for a single cell in response to repetitive burst stimulation. Green arrows indicate the onset of each stimulus, and red horizontal bar represents a period where no stimulus was delivered (D) Close up of two microcoils conformally placed on top of a mouse retinal slice in fluorescence mode (left) and heat-map of peak fluorescence change to stimulus(right). Purple circle indicates neuron in which fluorescence is analyzed below. (E) Schematic of burst stimulus waveform that was delivered to a single coil. Each burst consisted of 100 pulses, at 100mA pulse amplitude and 0.2ms duration, delivered at an interval of 5ms. (F) Calcium fluorescence change observed for a single cell in response to repetitive burst stimulation. Green arrows indicate the onset of each stimulus, and red horizontal bar represents a period where no stimulus was delivered. (G) Close up of a single 10kOhm microelectrode conformally placed on top of a mouse cortical slice in fluorescence mode (left) and heat-map of peak fluorescence change to stimulus(right). Yellow circle indicates neuron in which fluorescence is analyzed below. (H) Schematic of burst stimulus waveform that was delivered through the electrode. Each burst consisted of 20 pulses, at 70uA pulse amplitude and 0.2ms duration, delivered at an interval of 9.6ms. (I) Calcium fluorescence change observed for a single cell in response to a single stimulation burst stimulation. Green arrows indicate the onset of each stimulus, and red horizontal bar represents a period where no stimulus was delivered. Scale bar indicates 20 µm.

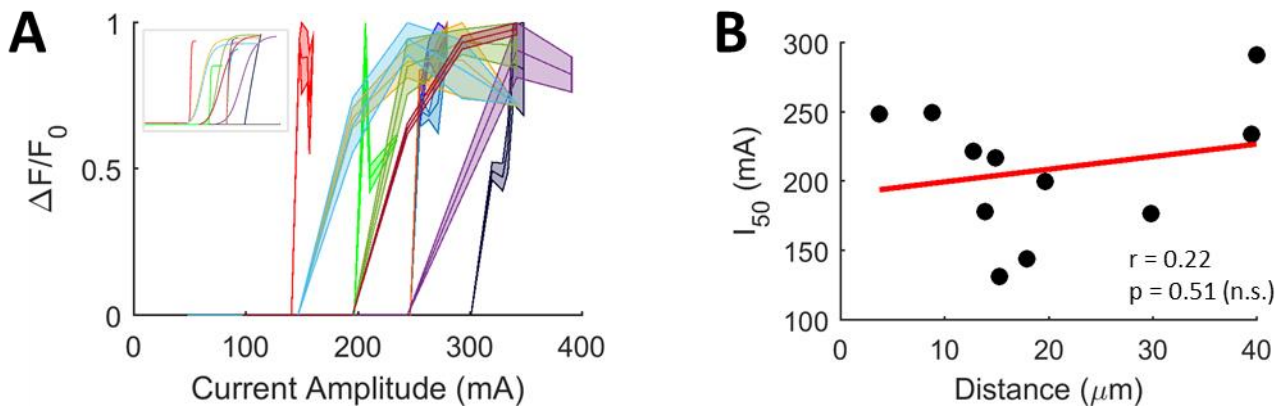

Figure 5: Cortical neurons are sensitive to stimulus amplitude. (A) Dose-response curves depict the relationship between amplitude of magnetic stimulation and (normalized) change in fluorescence of cortical neurons. Each color corresponds to a different cell (11 in total, 5 slices). Shaded error bars indicate the standard deviation across repeated trials (n = 3). *Inset:* Sigmoid fits for each dose-response curve. (B) Relationship between the distance from soma to coil tip and magnetic stimulation threshold (estimated as the current required to elicit 50% of the maximum fluorescence change). Line of best fit (red) and regression analysis are shown.

Discussion

As part of this study, we modeled, designed, microfabricated, and successfully validated the first generation of flexible, transparent, and conformal microcoil arrays for stimulation of CNS neurons. The V-shaped coil design was chosen for the array as result of computational modeling which revealed minimal overlap of electric field gradients in that shape as compared to the U-shaped and rectangular shaped geometries. Following this, we developed a 4 channel microcoil array design with spacing of 250 µm between tips which was based off of the approx. spacing

between adjacent cortical columns in the visual cortex. We successfully optimized a robust microfabrication protocol that was able to produce devices which consisted of a metal (Cu) layer sandwiched between two layers of SU-8. Once assembled, we performed functional validation of our devices through a series of bench experiments that confirmed that they were able to reliably generate electrical artifact signals which were consistent with the results from previous studies **(Lee et al., 2016)**. Following these bench experiments, we performed electrophysiology experiments in cortical tissue slices and retinal explants that demonstrated that the ability of our devices to successfully activate CNS neurons located very close to the microcoil tip (<50 µm). The activation patterns produced by our microcoil devices were quite different from that generated by microelectrodes, which activated a larger region of neuropil and somata. Further, we also found that cortical neurons have variable thresholds to magnetic stimulation, and that these thresholds were not correlated to distance from the microcoil tip. This raises interesting questions for future studies to (1) better evaluate additional factors which may be responsible for the variable cellular thresholds, and (2) patterns of activation that result from stimulation of multiple coils due to constructive and destructive interference of electric field gradients.

While the use of bioinert materials like SU-8 for chronic neural implants has been demonstrated to mitigate the adverse inflammatory responses that are usually associated with metal electrodes (Zhou et al., 2017; Yang et al., 2019), we have developed a general platform that may be extended to other bioactive materials (e.g silk) which could further minimize or eliminate tissue fibrosis. The use of photo-cross-linkable silk fibroin has been shown to exhibit greater affinity to cultured neurons than SU-8 in addition to being a comparable insulation material (Ju et al., 2020). In addition, electrodes with silk-based coatings and supports have demonstrated significantly reduced glial responses in both *in-vitro* and *in-vivo* applications (Tien et al., 2013; Lee et al., 2019) . Further, silk fibroin offers the added benefits of being mechanically tunable and the ability to be encapsulated with enzymes that can ameliorate scarring (Tien et al., 2013). It will be of interest for future studies evaluating the chronic stability, efficacy, and safety of microcoil based implants to examine differences between rigid and more flexible, bioinert /bioactive substrate materials.

While our current fabrication procedure allows for standard SU-8 geometries, it can be readily modified to produce more conformal interfaces using stretchable or injectable substrate

geometries. For example, work by Kim et al. (2011) and Zhang et al. (2013) (Kim et al., 2011; Zhang et al., 2013) have demonstrated that serpentine electrode interconnects incorporated within ultra-thin substrate materials can form extremely stretchable interfaces that can conform to different types of biological tissue, with modulus of elasticity that can range between 100 MPa to 300 kPa. Additionally, devices embedded in SU-8 have also achieved electrophysiological interfaces using complex 3D geometries (e.g, self-rolled spheroids) (Kalmykov et al., 2021). Finally, work from the Lieber group (Zhou et al., 2017) has shown that SU-8 can be used as a basis to create injectable mesh-like MEAs that can be smoothly be inserted into brain tissue and minimize the tissue damage that may occur during device insertion. These studies raise interesting possibilities for the next generation of flexible microcoil devices to enhance their conformability, stretchability, and ease of insertion for chronic applications.

In order to facilitate the clinical translation of our microcoil array for use as a neural implant, it will be necessary to modify the design so as to significantly increase the number of coil elements to improve its spatial acuity. A recent study performed in the visual cortex of primates demonstrated the ability of 1024 channel multi electrode array to successfully generate a range of visual percepts that consisted of simple shapes, motions, and letters which the monkeys were able to readily recognize (Chen et al., 2020). While techniques like that described above and in (Hong et al., 2018) can be used to fabricate high density meshes of stimulation elements, future *in-vivo* studies involving microcoil based arrays will need to determine the appropriate of channels and stimulation parameters that are needed to effectively elicit visual percepts.

Acknowledgements

Research was supported by BRAIN R01-NS110575 and DOD/CDMRP VR170089 to S.I.F.

References

Badi AN, Kertesz TR, Gurgel RK, Shelton C, Normann RA (2003) Development of a Novel Eighth-Nerve Intraneural Auditory Neuroprosthesis. The Laryngoscope 113:833–842 Available at: https://onlinelibrary.wiley.com/doi/abs/10.1097/00005537-200305000-00012 [Accessed March 29, 2019].

Basser PJ, Wijesinghe RS, Roth BJ (1992) The activating function for magnetic stimulation derived from a three-dimensional volume conductor model. IEEE Trans Biomed Eng 39:1207–1210.

Bonin V, Histed MH, Yurgenson S, Reid RC (2011) Local Diversity and Fine-Scale Organization of Receptive Fields in Mouse Visual Cortex. J Neurosci 31:18506–18521.

Bonmassar G, Lee SW, Freeman DK, Polasek M, Fried SI, Gale JT (2012) Microscopic magnetic stimulation of neural tissue. Nat Commun 3:921.

Butovas S, Schwarz C (2003) Spatiotemporal Effects of Microstimulation in Rat Neocortex: A Parametric Study Using Multielectrode Recordings. J Neurophysiol 90:3024–3039.

Chen X, Wang F, Fernández E, Roelfsema P (2020) Shape perception via a high-channel-count neuroprosthesis in monkey visual cortex. Science.

Cheung KC (2007) Implantable microscale neural interfaces. Biomed Microdevices 9:923–938 Available at: https://doi.org/10.1007/s10544-006-9045-z [Accessed March 29, 2019].

Deng Z-D, Lisanby SH, Peterchev AV (2013) Electric field depth-focality tradeoff in transcranial magnetic stimulation: simulation comparison of 50 coil designs. Brain Stimulat 6:1–13.

Esselle KP, Stuchly MA (1992) Neural stimulation with magnetic fields: analysis of induced electric fields. IEEE Trans Biomed Eng 39:693–700.

Fried SI, Lasker ACW, Desai NJ, Eddington DK, Rizzo JF (2009) Axonal Sodium-Channel Bands Shape the Response to Electric Stimulation in Retinal Ganglion Cells. J Neurophysiol 101:1972–1987.

Grill WM, Norman SE, Bellamkonda RV (2009) Implanted neural interfaces: biochallenges and engineered solutions. Annu Rev Biomed Eng 11:1–24.

Histed MH, Bonin V, Reid RC (2009) Direct activation of sparse, distributed populations of cortical neurons by electrical microstimulation. Neuron 63:508–522.

Hong G, Yang X, Zhou T, Lieber CM (2018) Mesh electronics: a new paradigm for tissue-like brain probes. Curr Opin Neurobiol 50:33–41.

Huang S-H, Lin S-P, Chen J-JJ (2014) In vitro and in vivo characterization of SU-8 flexible neuroprobe: From mechanical properties to electrophysiological recording. Sens Actuators Phys 216:257–265 Available at: http://www.sciencedirect.com/science/article/pii/S0924424714003008 [Accessed

March 22, 2019].

Jang J, Kim H, Song YM, Park J-U (2019) Implantation of electronic visual prosthesis for blindness restoration. Opt Mater Express 9:3878.

Janssen AM, Oostendorp TF, Stegeman DF (2015) The coil orientation dependency of the electric field induced by TMS for M1 and other brain areas. J NeuroEngineering Rehabil 12:47.

Ju J, Hu N, Cairns DM, Liu H, Timko BP (2020) Photo–cross-linkable, insulating silk fibroin for bioelectronics with enhanced cell affinity. Proc Natl Acad Sci 117:15482–15489.

Kalmykov A, Reddy JW, Bedoyan E, Wang Y, Garg R, Rastogi SK, Cohen-Karni D, Chamanzar M, Cohen-Karni T (2021) Bioelectrical interfaces with cortical spheroids in three-dimensions. J Neural Eng 18:055005.

Kim D-H et al. (2011) Epidermal Electronics. Science 333:838–843.

Kozai TDY, Jaquins-Gerstl AS, Vazquez AL, Michael AC, Cui XT (2014) Brain Tissue Responses to Neural Implants Impact Signal Sensitivity and Intervention Strategies. ACS Chem Neurosci 6:48–67 Available at: https://www.ncbi.nlm.nih.gov/pmc/articles/PMC4304489/ [Accessed March 30, 2019].

Larsch J, Ventimiglia D, Bargmann CI, Albrecht DR (2013) High-throughput imaging of neuronal activity in Caenorhabditis elegans. Proc Natl Acad Sci U S A 110:E4266–E4273.

Lecomte A, Descamps E, Bergaud C (2018) A review on mechanical considerations for chronically-implanted neural probes. J Neural Eng 15:031001.

Lee SW, Fallegger F, Casse BDF, Fried SI (2016) Implantable microcoils for intracortical magnetic stimulation. Sci Adv 2:e1600889.

Lee SW, Fried SI (2017) Enhanced Control of Cortical Pyramidal Neurons With Micromagnetic Stimulation. IEEE Trans Neural Syst Rehabil Eng 25:1375–1386.

Lee SW, Thyagarajan K, Fried S (2018) Micro-coil design influences the spatial extent of responses to intracortical magnetic stimulation. IEEE Trans Biomed Eng:1–1.

Lee Y, Kong C, Chang JW, Jun SB (2019) Carbon-Fiber Based Microelectrode Array Embedded with a Biodegradable Silk Support for In Vivo Neural Recording. J Korean Med Sci 34:e24.

Lewis PM, Ackland HM, Lowery AJ, Rosenfeld JV (2015) Restoration of vision in blind individuals using bionic devices: a review with a focus on cortical visual prostheses. Brain Res 1595:51–73.

Makarov SN, Wartman WA, Daneshzand M, Fujimoto K, Raij T, Nummenmaa A (2020) A software toolkit for TMS electric-field modeling with boundary element fast multipole method: an efficient MATLAB implementation. J Neural Eng 17:046023.

Matarèse BFE, Feyen PLC, Falco A, Benfenati F, Lugli P, deMello JC (2018) Use of SU8 as a stable and biocompatible adhesion layer for gold bioelectrodes. Sci Rep 8:5560 Available at: https://www.nature.com/articles/s41598-018-21755-6 [Accessed March 22, 2019].

Miranda PC, Hallett M, Basser PJ (2003) The electric field induced in the brain by magnetic stimulation: a 3-D finite-element analysis of the effect of tissue heterogeneity and anisotropy. IEEE Trans Biomed Eng 50:1074–1085.

Nemani KV, Moodie KL, Brennick JB, Su A, Gimi B (2013) In vitro and in vivo evaluation of SU-8 biocompatibility. Mater Sci Eng C Mater Biol Appl 33 Available at: https://www.ncbi.nlm.nih.gov/pmc/articles/PMC3843949/ [Accessed November 20, 2018].

Polikov VS, Tresco PA, Reichert WM (2005) Response of brain tissue to chronically implanted neural electrodes. J Neurosci Methods 148:1–18.

Raghuram V, Werginz P, Fried SI, Timko BP (2021) Morphological Factors that Underlie Neural Sensitivity to Stimulation in the Retina. Adv NanoBiomed Res n/a:2100069.

Raspopovic S, Valle G, Petrini FM (2021) Sensory feedback for limb prostheses in amputees. Nat Mater 20:925–939.

Rattay F (1986) Analysis of models for external stimulation of axons. IEEE Trans Biomed Eng 33:974–977.

Roth BJ, Basser PJ (1990) A model of the stimulation of a nerve fiber by electromagnetic induction. IEEE Trans Biomed Eng 37:588–597.

Ryu SB, Paulk AC, Yang JC, Ganji M, Dayeh SA, Cash SS, Fried SI, Lee SW (2020) Spatially confined responses of mouse visual cortex to intracortical magnetic stimulation from micro-coils. J Neural Eng 17:056036.

Salatino JW, Ludwig KA, Kozai TDY, Purcell EK (2017) Glial responses to implanted electrodes in the brain. Nat Biomed Eng 1:862–877 Available at: https://www.ncbi.nlm.nih.gov/pmc/articles/PMC6261524/ [Accessed March 15, 2019].

Song E, Li J, Won SM, Bai W, Rogers JA (2020) Materials for flexible bioelectronic systems as chronic neural interfaces. Nat Mater 19:590–603.

Tien LW, Wu F, Tang-Schomer MD, Yoon E, Omenetto FG, Kaplan DL (2013) Silk as a Multifunctional Biomaterial Substrate for Reduced Glial Scarring around Brain-Penetrating Electrodes. Adv Funct Mater 23:3185–3193.

Wagner T, Fregni F, Eden U, Ramos-Estebanez C, Grodzinsky A, Zahn M, Pascual-Leone A (2006) Transcranial magnetic stimulation and stroke: a computer-based human model study. NeuroImage 30:857–870.

Wang B, Grill WM, Peterchev AV (2018) Coupling Magnetically Induced Electric Fields to Neurons: Longitudinal and Transverse Activation. Biophys J 115:95–107.

Werginz P, Raghuram V, Fried S (2020) The relationship between morphological properties and thresholds to extracellular electric stimulation in α RGCs. J Neural Eng Available at: http://iopscience.iop.org/10.1088/1741-2552/abab47 [Accessed August 3, 2020].

Williams JC, Hippensteel JA, Dilgen J, Shain W, Kipke DR (2007) Complex impedance spectroscopy for monitoring tissue responses to inserted neural implants. J Neural Eng 4:410–423 Available at:

https://doi.org/10.1088%2F1741-2560%2F4%2F4%2F007 [Accessed April 4, 2019].

Yang X, Zhou T, Zwang TJ, Hong G, Zhao Y, Viveros RD, Fu T-M, Gao T, Lieber CM (2019) Bioinspired neuron-like electronics. Nat Mater 18:510–517.

Zhang Y, Xu S, Fu H, Lee J, Su J, Hwang K-C, Rogers JA, Huang Y (2013) Buckling in serpentine microstructures and applications in elastomer-supported ultra-stretchable electronics with high areal coverage. Soft Matter 9:8062–8070.

Zhou T, Hong G, Fu T-M, Yang X, Schuhmann TG, Viveros RD, Lieber CM (2017) Syringe-injectable mesh electronics integrate seamlessly with minimal chronic immune response in the brain. Proc Natl Acad Sci 114:5894–5899.